Article

Anti-Bacterial Iron Oxide Magnetic Nanoparticles based on Orange Peel Extract

David Giancarlo García Vélez [1], Cristina C. Garzón-Romero[3], Mateo Alejandro Salazar Salazar[3], Karina J. Lagos[1], Kleber Orlando Campaña Cruz[1], Alexis Debut[5], Karla Vizuete[5], Miryan Rosita Rivera [3], Dario Niebieskikwiat[4], Maria J. Benitez[2], María Paulina Romero Obando[1*].

[1]Department of Materials, Escuela Politécnica Nacional (EPN), Quito, Ecuador
[2]Departmento de Física, Escuela Politécnica Nacional (EPN), Quito, Ecuador
[3]Laboratorio de Investigación en Citogenética y Biomoléculas de Anfibios (LICBA), Centro de Investigación para la Salud en América Latina (CISeAL), Facultad de Ciencias Exactas y Naturales, Pontificia Universidad Católica del Ecuador (PUCE), Quito, Ecuador
[4]Department of Physics, Colegio de Ciencias e Ingenierías, Universidad San Francisco de Quito, Quito, Ecuador.
[5] Centro de Nanociencia y Nanotecnología, Universidad de Las Fuerzas Armadas ESPE, Sangolquí 171103, Ecuador
* Correspondence: maria.romerom@epn.edu.ec

Abstract: Magnetic nanoparticles based on iron oxides (MNPs-Fe) with magnetite or maghemite phases have been widely employed in bio-applications. Thus, they have been used as contrast agents in magnetic resonance imaging (MRI) and oncological treatments through different therapies. Besides, due to the vast health problem of multidrug-resistant bacterial infections, several studies have proposed MNPs-Fe as photothermal agents (PTAs) within antibacterial photothermal therapy (PTT). This work presents a quick and easy green synthesis (GS) to obtain MNPs-Fe using orange peel extract from orange waste from local commerce, which presents an environmentally friendly approach compared to traditional methods such as coprecipitation. The GS can be irradiated with microwaves to reduce the synthesis time drastically. We evaluated the weight yield of the GS and the physical-chemical and magnetic features of the synthesized MNPs-Fe. Besides their cytotoxicity in animal cell line ATCC RAW 264.7, their antibacterial activity against *Staphylococcus Aureus (S. Aureus)* and *Escherichia Coli (E. Coli)* was assessed. We found that the MNPs-Fe synthesized using the GS, with 50% v/v of NH_4OH and 50% v/v of orange peel extract (50GS-MNPs-Fe) had an excellent weight yield, negligible cytotoxicity for concentrations of MNPs-Fe below 250 $\mu g \cdot mL^{-1}$ in 24 hours, and 8 days. In the MNPs-Fe surface, we identified a coating of organic molecules (~ 25 nm) such as terpenes, aldehydes, *etc*. MNPs-Fe inhibited *S. Aureus* and 2.54 $\log_{10}$ (CFU) of *E. Coli* under red LED light irradiation (630 nm, 65.5 $mW \cdot cm^{-2}$, 30 min). Likewise, they exhibited a superparamagnetic (SPM) behavior for temperatures above 60 K, with a size of 49.3±9.6 nm and saturation magnetization (Ms) of 72.83 and 44.16 $emu \cdot g^{-1}$ at 60 and 300 K, respectively. Therefore, 50GS-MNPs-Fe are excellent candidates as broad-spectrum PTAs in antibacterial PTT, magnetic hyperthermia (MH), or MRI.

Keywords: Green synthesis; antibacterial PPT; iron oxide nanoparticles; orange peel extract; cytotoxicity; superparamagnetic behavior.

1. Introduction

Bacterial infections are the potential cause for developing chronic infections in patients, producing severe health problems and death (1). These infections are typically treated with antibiotics, but their uncontrolled use (dosage and chemical modification) has led to bacteria growing drug resistance (2–4), either through bacterial survival mechanisms (exchange of resistant genes) or in biofilm conditions (5). Bacterial strains can proliferate on most solid surfaces, *e.g.*, prosthetics catheters, medical equipment, hospital

Preprints (www.preprints.org) | NOT PEER-REVIEWED | Posted: 23 December 2022 doi:10.20944/preprints202212.0436.v1

ventilation ducts, open wounds, walls of the respiratory system, food, food packaging, *etc.* (6). For this reason, multidrug-resistant (MR) bacterial infections are considered one of the three primary health problems of the 21st century, which will cause 300 million deaths with an economic loss greater than $ 100 trillion in the next 28 years (7).

Nanotechnology has contributed to finding solutions to bacteria elimination problems, *e.g.*, carbon-based materials such as graphene oxide (GO), reduced graphene oxide (r-GO), carbon dots (CDs), and carbon nanotubes (CNTs) (5). Also, metal nanoparticles (NPs) such as AgNPs, AuNPs, PtNPs, *etc.*, (8) and metal oxide NPs like magnetite (Fe_3O_4) and maghemite (γ-Fe_2O_3) (9) have been employed to combat this problem due to their intrinsic antibacterial activity and, according to their nature, they can inhibit gram-positive and gram-negative bacteria by different mechanisms (1,10–12). In several cases, the antimicrobial activity of the cited nanomaterials can be enhanced with functionalizing agents (antibiotics, polymers, organic molecules, *etc.)* (13–15) or by incorporating therapies such as photodynamic therapy (PDT) and PTT (16–18). Iron oxides such as magnetite and maghemite are made of iron (Fe^{+2}, Fe^{+3}) and oxygen (O^{-2}) ions in a spinel-inverse crystallographic arrangement, producing ferrimagnetic behavior (19,20). MNPs-Fe, such as magnetite or maghemite, exhibited interesting properties like SPM behavior, quantum tunneling, high specific surface, low cytotoxicity, biocompatibility, and biodegradability, among others (9,21,22). It is essential to highlight the capability of manipulating MNPs-Fe motion by magnetic fields (23). Therefore, MNPs-Fe has generated significant interest in biomedical applications such as targeted drug delivery, MRI, and oncological therapies such as MH, PDT, and PTT (22,24,25). However, the Food and Drug Administration (FDA) approves using MNPs-Fe in clinical applications, mainly as a replacement source of iron, *e.g.*, Ferumoxytol®, in MRI (Feridex® /Endorem™, GastroMark™, Umirem®) and MH (Nanotherm®) (4,26,27). According to FDA protocols, some nanocomposites of MNPs-Fe, such as Combidex®, Resovist®, and Ferrotran®, are in the approval phase for MRI (28).

Antibacterial PTT uses light irradiation, typically in the near-infrared (NIR, 700-1350 nm, optical window) (29), to raise the temperature ~ 50 °C of PTAs (30,31), which host bacteria cell membranes or internalize by several mechanisms like passive diffusion, receptor-mediated endocytosis, among others (1,32,33), causing irreversible damage in the cell membrane and protein disruption which leads to bacterial death (16). When using MNPs-Fe as PATs, a characteristic effect is achieved known as Localized Surface Plasmonic Resonance (LSPR). The electric field of NIR light induces collective resonant oscillation of free electrons (electron cloud) of the MNPs-Fe, due to the absorbed photons, which are converted into phonons, increasing the temperature in the crystal lattice of the MNPs-Fe (31). For this reason, MNPs-Fe are excellent candidates as broad-spectrum antibacterial agents in antibacterial PTT (4,34).

In the human body, endocytosis is a key mechanism by which cells interact with large or small particles. The phagocytes use their plasma membrane to engulf NPs (phagocytosis) or, in turn, are inhibited by forming a crown of non-specific proteins, producing unpredictable pharmacokinetics (35). Thus, their size, morphology, and surface chemistry play an essential role in the interaction with target cells; *e.g.*, the kidneys remove size NPs < 10 nm, and the liver removes size NPs > 10 nm, which can also be phagocytized (33,34). To improve the availability of NPs in the biological environment, they typically are functionalized with polymeric molecules such as polyethylene glycol (PEG), which produces a protein repulsion effect; or molecules of interest that allow increasing selectivity toward target cells (26). In the case of MNPs-Fe, their SPM behavior makes the magnetic targeting towards the required zone possible. Still, surface chemistry and size govern the interaction between the MNPs-Fe and the target cell (14). It should be pointed out that the MNPs-Fe prepared from the orange peel or other natural wastes have functional groups or organic molecules which come from the same orange peel or the natural waste used. To achieve SPM behavior, the uniform size distribution (< 100 nm) of the MNPs-Fe and a non-interacting system are essential, *i.e.*, an adequate concentration of MNPs-Fe that does not allow the formation of agglomerates and the MNPs-Fe not interacts with each other by its proximity (36). Avoiding the agglomeration of NPs is an intrinsic challenge present in the

 doi:10.20944/preprints202212.0436.v1

synthesis routes of nanomaterials and makes it difficult to develop bio-applications adequately (37).

The toxic effect of MNPs-Fe at a cellular level (cytotoxicity) has been studied in healthy eukaryotic cells (*e.g.*, fibroblasts, liver cells, stem cells derived from adipose tissue, *etc.*)(38,39) and diseased cells (mainly cancer cells, *e.g.*, DU -145, LNcaP, HeLa, MCF-7, *etc.*) (9,40,41), as well as in prokaryotic cells, *e.g.*, *S. Aureus*, *E. Coli*, and so on (toxic effect on bacteria known as antibacterial activity) (12,14,42). In any case, the cytotoxic effect depends on the concentration of the MNPs-Fe. Similar mechanisms of cell damage are present in prokaryotic and eukaryotic cells. The MNPs-Fe induce oxidative stress by generating reactive oxygen species (ROS). It releases Fe ions (Fe^{+2}, Fe^{+3}) that create an acidic environment and, in the presence of H_2O_2, produce $^{\bullet}OH$ radicals (Fenton reaction) that depolymerize polysaccharides, inactivate enzymes, lipid peroxidation, and DNA damage. MNPs-Fe can also cause mechanical disruption by localizing to the cell membrane (14,43).

The MNPs-Fe are obtained by different synthesis methods, which allow controlling the morphology, size, and surface chemistry of the MNPs-Fe. These routes rank among physical, chemical, and biological synthesis methods (15). By chemical synthesis methods, homogeneous products can be obtained due to better control of parameters such as temperature, aliquots of precursors, and pressure, among others (44). Typical chemical synthesis methods of MNPs-Fe are coprecipitation (45), sol-gel (46), hydrothermal (47), and solvothermal (48), among others (49–51). Nevertheless, these synthesis methods usually involve potentially toxic reagents, resulting in environmental and biological risks (24).

The green synthesis (GS) of MNPs-Fe proposes reducing or replacing the conventional agents that are dangerous in their handling and has toxic composition, *e.g.*, ammonium hydroxide (NH_4OH) or sodium hydroxide (NaOH) (52–55), with plant extracts obtained from leaves, fruits, seaweeds, and so on (56). These extracts have functional groups that act as reducing agents and stabilizing agents in the formation of the MNPs-Fe (57). Hence, the GS becomes easy and friendly to the environment (58). Plant extracts incorporate the circular economy concept in obtaining MNPs-Fe, due to the use of organic waste from the food industry (59). It is possible in GS to incorporate heating by microwave (MW) irradiation, achieving higher reaction rates and thus reducing synthesis times due to rapid and homogeneous volumetric heating (rotation of electric dipoles and ions) compared to conventional heating methods, *e.g.*, heating by flame or electric resistance (21,60–62).

This work presents a quick and easy GS to obtain MNPs-Fe using MW irradiation and iron precursors, ammonium hydroxide, and orange peel extract from orange waste produced by street orange juice vendors. The orange peel constitutes a reducing agent in combination with low amounts of ammonium hydroxide. To compare the properties of the as-prepared MNPs-Fe, we also carried out different syntheses using the coprecipitation (CO) method and irradiating with MW without plant extract. It evaluated the antibacterial activity within PTT, cytotoxicity, SPM behavior, weight yield of GS, and the effects (synthesis waste) of organic molecules of orange peel extract compared to the other MNPs-Fe obtained by CO and MW without plant extract.

2. Results and Discussion

2.1. Weight yield of MNPs-Fe

The quantification of the yield in weight is essential to evaluate the potential scaling of the synthesis at an industrial level. To obtain weight yield curves of the GS, CO, and MW synthesis (from the weight of the precursors and the MNPs-Fe obtained), dried the MNPs-Fe samples as indicated in section 2.3 and carried out triplicate tests. Figure 1 presents the average weights for each synthesis, and it can consult in detail in Table S1. The results indicated that GS has higher weight yields of MNPs-Fe for NH_4OH (% v/v) between ~ 50 to 100 % v/v. The 100GS-MNPs-Fe and 100MW-MNPs-Fe samples are the same, *i.e.*, they had 100 % v/v of NH_4OH and were synthesized under the same conditions without orange peel extract. In NH_4OH (% v/v) between 0 to ~ 50 % v/v, the GS yield is considerably reduced compared to CO and MW, which maintain their yield. However, the

Preprints (www.preprints.org) | NOT PEER-REVIEWED | Posted: 23 December 2022 doi:10.20944/preprints202212.0436.v1

role of the organic molecules of the orange peel extract as a reducing agent stands out because, in the absence of NH_4OH, 0GS-MNPs-Fe were achieved in small quantities (8.97±2.32 mg). In turn, at 0 % v/v of NH_4OH in CO, MW did not crystallize MNPs-Fe. Only DI water was added to the precursor solution, reducing its concentration without generating any reaction.

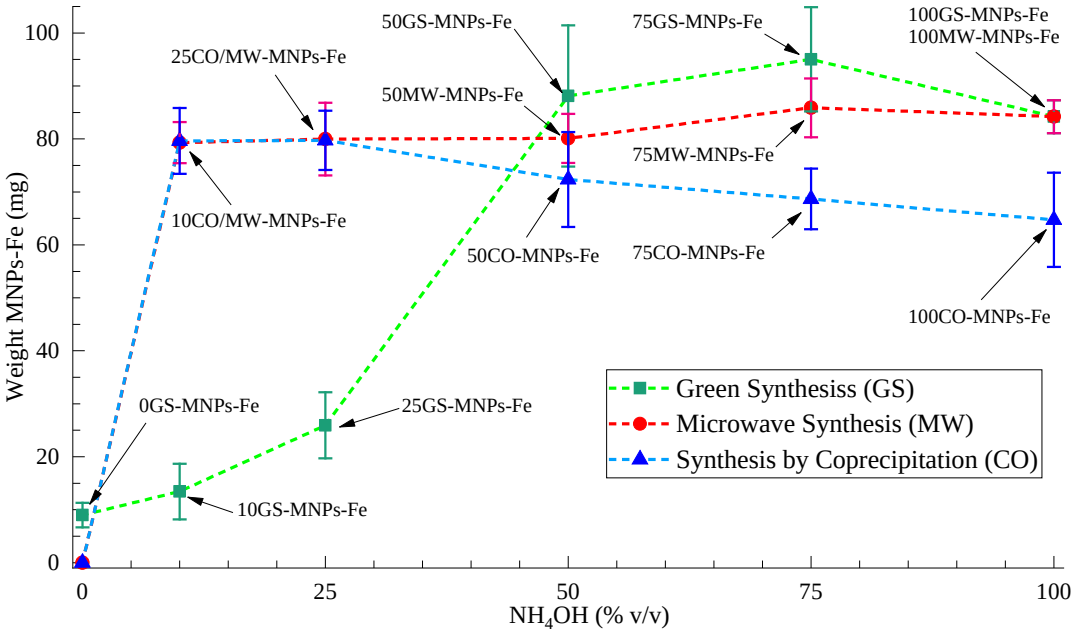

Figure 1. Weight yield curves for GS, CO, and MW according to the NH4OH (% v/v).

It is essential to indicate that the magnetic character of the sample 0GS-MNPs-Fe was not stable, *i.e.*, this solution lost its magnetic character in short periods (24-48 hours). The low stability of 0GS-MNPs-Fe can occur due to the oxidation of the magnetite and maghemite on the surface of a large number of organic molecules available (100 % v/v of orange peel extract), as suggested by Lopez G. *et al*. (68).

In GS, it is complex to establish a formation reaction of the MNPs-Fe owing to the great variety of organic compounds in the orange peel extract, considering that these differ according to the place and period of the orange harvest (24,69). It is known that Fe^{+2} and Fe^{+3} ions form intermediate compounds such as $Fe(OH)_2$ and $Fe(OH)_3$ to generate Fe_3O_4 and water (70). Hence, the availability of OH^- ions in the reducing agent's solutions is crucial in synthesizing MNPs-Fe. For this reason, the pH (function of the H^+ concentration) in the reducing agent's solutions and the byproducts of the synthesis (GS, CO, and MW) were studied (see Figure S1). The acid character of the orange peel extract (pH=5.15) did not significantly influence the pH of the reducing agent´s solutions in GS, and it remained between 11.59 - 13.16 for solutions between 10-100 % v/v of NH_4OH, *i.e.*, a similar availability of hydroxyl ions (OH^-) in any case (CO and MW). Likewise, GS and MW product pH measurements were more environmentally friendly (pH=7.20 - 8.76) than CO (pH=9.74 - 11.11). The pH measurements were consistent with the yield of GS and MW since the synthesis consumed a more significant amount of OH^- ions to form MNPs-Fe. However, in GS, for 0 to ~ 50 %v/v of NH_4OH, a significant amount of available organic molecules can interact with the OH^- reducing the weight yield of MNPs-Fe. In the specific case of 0GS-MNPs-Fe, the byproducts were acidic (pH=1.52) because the few available OH^- were consumed, increasing the concentration of H^+.

Equation 1 proposes a possible mechanism for the formation of MNPs-Fe by GS according to the precursors and reducing agents used in this work, where the quantity and type of molecules from the orange peel extract is a factor that influences the weight yield of MNPs-Fe. Equation 1 was adjusted from the proposal made by Palash D. *et al*. (58), who used *Lathyrus sativus* peel extract.

Preprints (www.preprints.org) | NOT PEER-REVIEWED | Posted: 23 December 2022 doi:10.20944/preprints202212.0436.v1

$$Fe^{+3} + 3Cl^{-1} + Fe^{+2} + SO_4{}^{-2} + OH^- + NH_4^+ + NH_3 + orange\ peel\ extract + H_2O \xrightarrow{Microwave} Fe_3O_4 + \gamma - Fe_2O_3 + byproducts \quad (1)$$

The sample 50GS-MNPs-Fe was selected to develop the cytotoxicity and antibacterial PTT studies for their high weight yield (88.13±13.33 mg) and low NH_4OH consumption (greater green approach) compared to samples 75GS-MNPs-Fe (95.03±9.85 mg) and 100GS-MNPs-Fe (84.20±3.10 mg). In addition, its weight yield was approximately 50MW-MNPs-Fe (80.10±4.61 mg) and 50CO-MNPs-Fe (72.33±8.96 mg), which did not occur for lower 50% v/v of NH_4OH.

To have comparative results, the mass yield of Fe was calculated from the amount of Fe in the precursors and the Fe present in the obtained MNPs-Fe and are shown in Table 1. The results acquired in XRD and EDS were considered.

Table 1. Mass yield of the synthesis GS, MW, and CO according to the Fe conversion.

Mass yield of the synthesis according to the Fe conversion.		
0GS-MNPs-Fe	1.12%	35.3 % Magnetite, 64.7 % Hematite
25GS-MNPs-Fe	3.71%	39.5% Magnetite, 53 % Maghemite
50GS-MNPs-Fe	29.36%	47% Magnetite, 53% Maghemite
75GS-MNPs-Fe	18.40%	47% Magnetite, 53% Maghemite
100GS-MNPs-Fe	91.50%	6.6% Magnetite,93.4 % Maghemite
25Co-MNPs-Fe	89.08%	88% Magnetite,12 % Maghemite
50Co-MNPs-Fe	80.15%	63.5% Magnetite, 36.5% Maghemite
75Co-MNPs-Fe	74.69%	8.9% Magnetite, 91.1% Maghemite
100Co-MNPs-Fe	72.56%	98% Magnetite,2 % Maghemite
25MW-MNPs-Fe	87.73%	34.1 % Magnetite,65.9 % Maghemite
50MW-MNPs-Fe	89.59%	91.2% Magnetite, 8.8% Maghemite
75MW-MNPs-Fe	93.43%	10% Magnetite, 90% Maghemite

The weight yields of the synthesis by CO and MW were similar to those reported in analogous studies (62-97%) (71–73) that use Fe salt-type precursors. GS generated low yields by weight (1.12-29.36 %), except for the 100GS-MNPs-Fe sample (without extract). This stands out with the results reported by E. Nnadozie *et al*. (3-85%) (74). However, in the synthesis we propose in this study, the synthesis time is considerably reduced (a few minutes) compared to the 14 days reported by E. N *et al*., which includes drying *Chromolaena odorata* leaves, used as a green extract. This is due to using microwaves and vegetable extract in the liquid state. Likewise, reducing the amount of magnetic phase allows the incorporation of organic molecules, which provide additional benefits to our Fe-MNPs.

2.2. MNPs-Fe characterization

2.2.1. Morphology, size distribution and topography of MNPs-Fe

The SEM images of the samples obtained by GS allowed us to identify a quasi-spherical morphology and a normal size distribution, see Figure S2. The 50GS-MNPs-Fe sample had an average size of 49.3±9.6 nm, the smallest of the GS samples (see Figure 2a). A few agglomerates were also found and neglected to determine the average size of the MNPs-Fe. DLS allowed to study of the hydrodynamic diameter of the 50GS-MNPs-Fe samples, and two populations of different sizes were observed, see Figure 2b. In DLS, a model based on the intensity of the scattered electric field for polydisperse particles was used, which presents intensity contributions according to the hydrodynamic radius of the populations present. Thus, it is highlighted that the highest intensity does not refer to the population quantity of MNPs-Fe (75). This result corroborates that the few agglomerates observed in SEM comprised the 224.8±0.4 nm population. The 74.7±0.1 nm population corresponds to the 50GS-MNPs-Fe size coated with organic molecules from the orange peel extract, which is consistent with the study developed by Bano S. *et al*. (24). This shell of organic molecules has a thickness of 25.4 nm, as indicated in Figure 2b. It is necessary to highlight that the SEM images show the naked MNPs-Fe.

Preprints (www.preprints.org) | NOT PEER-REVIEWED | Posted: 23 December 2022 doi:10.20944/preprints202212.0436.v1

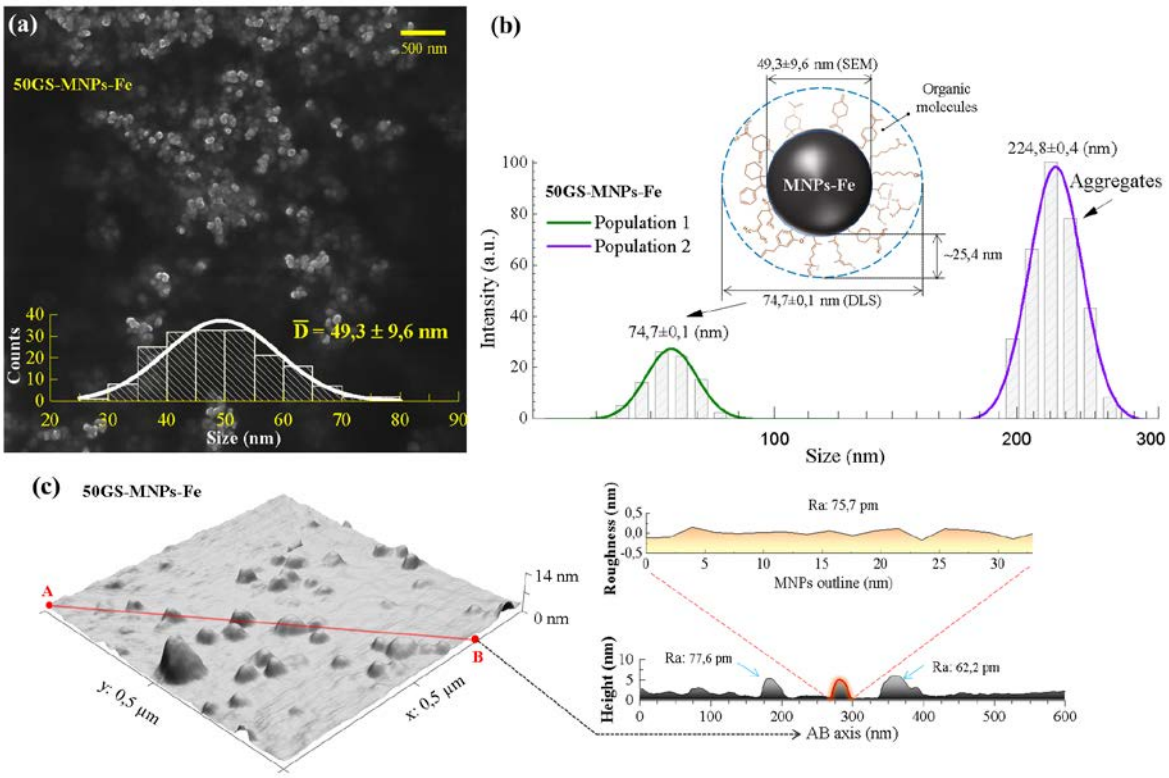

Figure 1. a) SEM images of 50GS-MNPs-Fe, b) Hydrodynamic size distribution of the 50 GS-MNPs-Fe samples obtained by DLS, and c) AFM image of the 50GS-MNPs-Fe sample and two-dimensional profiles obtained from the AFM topography with the Gwyddion 2.60 software.

The AFM topography of the GS samples enabled to study of the average roughness (Ra) of the MNPs-Fe and corroborated a quasi-spherical morphology. Figure 2c corresponds to the topography of the 50GS-MNPs-Fe sample. The contours of the MNPs-Fe (red curve) in two-dimensional profiles along an arbitrary axis (*e.g.*, AB axis in Figure 2c) acquired from Gwyddion 2.60 software empowered us to study Ra. Consequently, 20 random measurements of Ra were achieved in different contours and profiles of the MNPs-Fe, omitting regions of agglomerates and without MNPs-Fe. To estimate a representative Ra of the scanned section, Ra was measured in 20 profiles of the MNPs-Fe. This was achieved by taking AB axes randomly, which comprise different MNPs-Fe and avoiding agglomerates. The values of Ra increased according to the amount of orange peel extract used in GS, see Table S2. The 50GS-MNPs-Fe sample showed a Ra= 78±22 pm, while 100GS-MNPs-Fe (without orange peel extract) exhibited a Ra=58±12 pm. Thus, in GS, the shell of MNPs-Fe formed by organic molecules from the orange peel extract increases the value of Ra. Furthermore, it is essential to consider that the Ra values are sensitive to pixel resolution and size (76). Likewise, Ra can be affected by the interaction between the AFM tip (Tapping mode) and the organic molecules bound to the MNPs-Fe since this superficial organic crown is approximately 24.2 nm (DLS) and can be considered a soft sample, as suggested by Christensen M. *et al*. (77).

2.2.2. Phase and chemical composition of the MNPs-Fe

The diffraction patterns of the MNPs-Fe, obtained by GS, MW, and CO, presented phases of magnetite (Fe_3O_4) and maghemite (Fe_2O_3). Their relative peak positions (2θ) most coincided with crystallographic charts reported in the Crystallography Open Database (COD) to magnetite; see Figure S3a-S3c. Nevertheless, the characteristic peaks of the organic molecules shell in these samples could reduce the intensity of the characteristic peaks of magnetite (13). The XRD patterns of the samples obtained by CO and GS

Preprints (www.preprints.org) | NOT PEER-REVIEWED | Posted: 23 December 2022 doi:10.20944/preprints202212.0436.v1

presented relative peak positions and intensities coinciding with the COD crystallographic charts because these MNPs-Fe do not have an organic shell, see Figures S4b and S4c.

Figure 3a shows the patterns obtained by XRD of 50GS-MNPs-Fe, 50MW-MNPs-Fe, and 50CO-MNPs-Fe samples. In the three cases, the characteristic peaks of magnetite and maghemite were observed at 2θ: 18.4° (111), 30.2° (220), 35.5° (311), 37° (222), 43.1° (400), 53.4° (242), 57.1° (511), 62.8° (440), 74.1° (533) and 89.5° (713) (78,79), matching the crystal charts COD. The 50GS-MNPs-Fe sample corresponded to magnetite 96-101-1033 COD and maghemite 96-900-6317 COD with a contribution of 47% and 53%, respectively. The 50MW-MNPs-Fe sample was identified as magnetite 96-900-5843 COD and maghemite 96-900-6318 COD, with a contribution of 91.2% and 8.8%, respectively. Likewise, the 50CO-MNPs-Fe sample coincided with magnetite 96-900-2320 COD and maghemite 96-900-6318 COD in a contribution of 63.5% and 36.5%, respectively. This identification was carried out in the Match! 3 software.

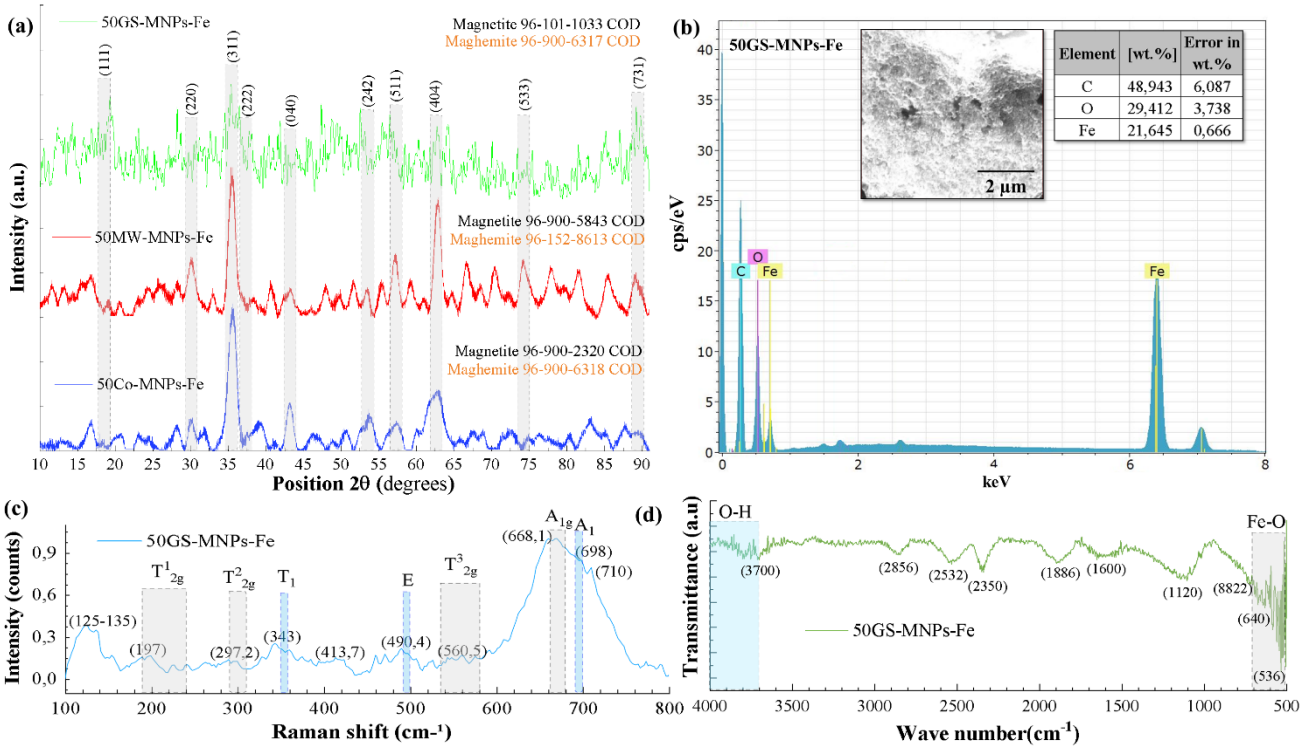

Figure 2. a) XRD patterns of samples of 50GS-MNPs-Fe, 50MW-MNPs-Fe, and 50CO-MNPs-Fe, b) EDS spectrum and elemental composition (wt. %) of the 50GS-MNPs-Fe sample, c) Raman spectrum between 100-800 cm^{-1} of the 50GS-MNPs-Fe sample, d) FT-IR spectrum of the 50GS-MNPs-Fe sample.

The XRD pattern of 50GS-MNPs-Fe shows many additional peaks. These peaks might correspond to organic molecules of the orange peel extract (MNPs-Fe shell), which have a crystalline structure, for example, crystalline cellulosic components with characteristic peaks at 2θ: 15°, 22°, and 35° (80). Likewise, compounds like Linalool and Eugenol reported in orange peel (24,69) have characteristic peaks at 2θ: 11.7°, 15.7°, 17.2°, 21.4°, 22.5°, 23.6°, and 30.2° (81).

The EDS elemental analysis (Figure 3b) allowed identifying the presence of carbon (C), Oxygen (O), and iron (Fe) in the 50GS-MNPs-Fe samples. The high weight percentages of C (48.847±6.087%), O (29.298±3.7%), and Fe (21.487±0.666%) were consistent with the XRD results, *i.e.*, magnetite, maghemite phases and a shell of carbon-based organic molecules. In the samples obtained by GS, the C content (wt. %) increased according to the amount of orange peel extract used in the synthesis, see Figure S4.

Preprints (www.preprints.org) | NOT PEER-REVIEWED | Posted: 23 December 2022 doi:10.20944/preprints202212.0436.v1

Raman spectra was acquired in the range of 100-2000 cm^{-1}. Nonetheless, the active Raman bands for magnetite and maghemite are within 100-800 cm^{-1} (53,54). Therefore, Figure 3c shows the Raman spectrum of the 50GS-MNPs-Fe sample in 100-800 cm^{-1}. The gray regions correspond to characteristic Raman bands of magnetite, and the light blue ones to characteristic bands of maghemite (85,86). Active bands of magnetite were observed at 197 cm^{-1} (T_{2g}^{1}, translational movement of the Fe_3O_4 structure), 297.2 cm^{-1} (T_{2g}^{2}, asymmetric stretching of Fe and O), 560.5 cm^{-1} (T_{2g}^{3}, asymmetric bending of O with respect to Fe), and 668.1 cm^{-1} (A_{1g}, symmetric stretching of O along Fe-O bonds) consistent with reports of active bands of magnetite (49). Likewise, the maghemite active bands observed are 343 cm^{-1} (T_1, asymmetric stretching Fe-O), 490.4 cm^{-1} (E, symmetric bending O along Fe-O bonds), and 698 cm^{-1} (A_1, symmetric stretching Fe-O) similar to the bands reported in (87,88). The bands 125-135 cm^{-1} correspond to the vibration of crystalline structures (LA-Modes) (89). The band observed at 413.7 cm^{-1} was attributed to the symmetrical stretching between O external to magnetite and maghemite with Fe ions belonging to iron oxides (89). The Raman spectrum of the 50GS-MNPs-Fe sample was compared to magnetite (record ID 319 obtained from the HORIBA database), generating a 79.32% correlation with the help of Wiley Science's KnowItAll software.

The complete Raman spectrum (See Figure S5) allowed identifying active bands of molecules bonds that cover the 50GS-MNPs-Fe sample (derived from orange peel extract). Table S3a shows the Raman active bands observed, with their molecular vibrations according to atomic bonds and the possible molecules present.

Figure 3d shows the FT-IR spectrum of the 50GS-MNPs-Fe sample. Active bands were observed between 600-450 cm^{-1}, corresponding to vibrations between Fe-O atoms of the magnetite and maghemite phases (90–93). Organic molecules' active FT-IR bands were also observed and shown in Table S3b. The FT-IR active band at 2532 cm^{-1} (S compounds) can be generated by ions ($SO4^{-2}$) derived from iron II sulfate. Likewise, the halogens are due to ions (Cl-1) from Fe III chloride used as a precursor. Also, the 2350 cm^{-1} band of amine salts suggests the formation of compounds derived from NH_4OH.

Tables S3a-b were developed according to the active bands reported by Horiba J. (89) for the analysis of Raman and FT-IR spectra, as well as the studies carried out by S. Bano *et al*. (24) and G. Kahrilas *et al*. (69).

Using FT-IR and Raman spectroscopy, the presence of magnetite and maghemite was corroborated, as well as the functionalization of the 50GS-MNPs-Fe with organic molecules of the type, alcohols, aldehydes, S compounds, amines, ketones, aromatic rings, halogens, and terpenes.

2.2.3. Magnetometry

Figure 4a shows M vs. H curves of the samples 50GS-MNPs-Fe, 50MW-MNPs-Fe, and 50CO-MNPs-Fe at different temperatures (60 K, 62 K, 65 K, and 300 K). The zoom at 300 K (upper left box) indicates almost zero Remanent Magnetization (Mr), as well as a coercivity (Hc) close to zero in all samples. The zoom at 60 K (lower right box) indicates higher Mr and Hc in the 50MW-MNPs-Fe and 50CO-MNPs-Fe samples. Nonetheless, the Mr and Hc of the 50GS-MNPs-Fe sample remain close to zero. This behavior and the Langevin-type curves suggest that at 300 K, all the samples exhibit an SPM behavior, and by reducing the temperature to 62 K and 65 K in the 50CO-MNPs-Fe and 50MW-MNPs-Fe samples, respectively, cross the blocking temperature (T_B) to a blocked state. Even so, the 50GS-MNPs-Fe sample maintains its SPM behavior, where the magnetic phase corresponded to 4.05 g of magnetite and maghemite in the sample, and the rest (9.35) to the coating of organic molecules. Figure 4b indicates that reducing the temperature in the 50CO-MNPs-Fe, and 50MW-MNPs-Fe samples increase Hc, indicating the opening of the M vs. H magnetization curves, which generates hysteresis. In contrast, in the 50GS-MNPs-Fe sample, the M vs. H curve remains closed with SPM behavior.

Preprints (www.preprints.org) | NOT PEER-REVIEWED | Posted: 23 December 2022 doi:10.20944/preprints202212.0436.v1

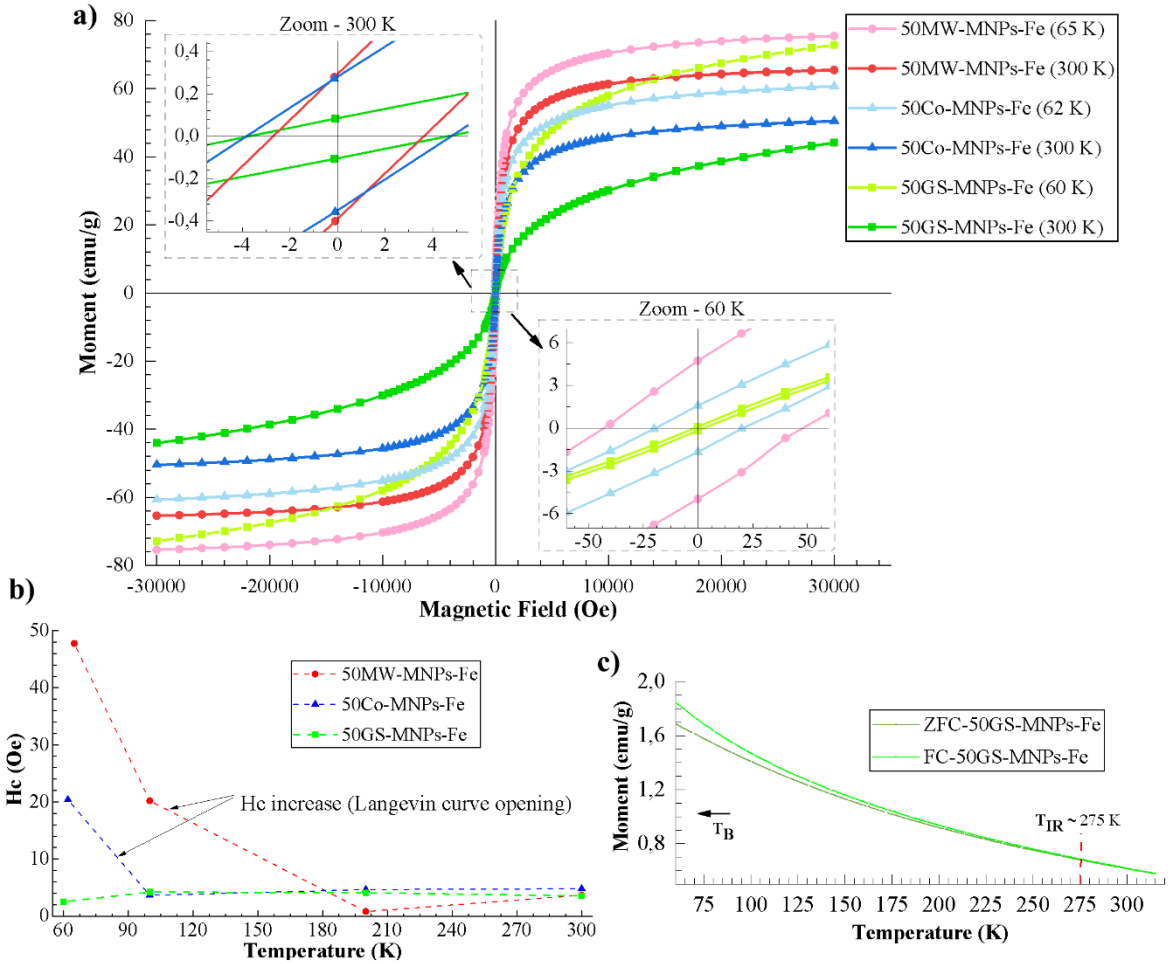

Figure 3. a) M vs. H curves of the samples 50GS-MNPs-Fe, 50MW-MNPs-Fe, and 50CO-MNPs-Fe at different temperatures (60, 62, 65, and 300 K), b) Hc vs. Temperature curves of 50GS-MNPs-Fe, 50MW-MNPs-Fe, and 50CO-MNPs-Fe samples, c) ZFC/FC curves of 50GS-MNPs-Fe sample.

The Ms of the 50MW-MNPs-Fe sample is the highest, being 65 emu·g^{-1} at 300K and 75.45 emu·g^{-1} at 65 K; followed by the values of the 50CO-MNPs-Fe sample (50.53 emu·g^{-1} at 300 K, 60.72 emu·g^{-1} at 62 K) and finally those from the 50GS-MNPs-Fe sample with a Ms of 44.16 emu·g^{-1} at 300 K and 72.83 emu·g^{-1} at 60 K. This result can be explained due to the 50MW-MNPs-Fe sample has the greatest magnetite phase (91.2%) as observed in XRD, followed by the 50MW-MNPs-Fe sample (63.5%) and then by the 50GS-MNPs-Fe sample (47%), which is consistent with the reported Ms of magnetite in the bulk state (90-92 emu·g^{-1} at 300 K) (94–96) and maghemite (30-80 emu·g^{-1} at 300 K) (97). This reduction in Ms is also affected by the greater surface anisotropy (nanometric scale) and especially for the 50GS-MNPs-Fe sample, by the presence of non-magnetic elements such as C, Cl, Al, and Si identified by EDS spectroscopy, which can cause distortions in the crystalline structure.

Figure 4c presents the ZFC and FC curves of the 50GS-MNPs-Fe sample and indicates that the temperature of T_B (transition from an SPM state to a blocked state) is below 60 K since no inflection is observed in the ZFC curve (operating capacity of the VSM), taking the criterion that the maximum peak of the ZFC curve corresponds to TB (98). The irreversibility temperature (T_{ir}) identified at 275 K (superposition of ZFC and FC curves) suggests a broad size distribution of the 50GS-MNPs-Fe (99), which is consistent with the presence of aggregates in the samples. The T_B of the 50MW-MNPs-Fe and 50CO-MNPs-Fe samples were determined at 211.1 K and 160.09 K, respectively. See Figure S6. Therefore, the 50GS-MNPs-Fe with SPM behavior can be used in applications that occur at temperatures greater than 60 K and below the Curie temperature.

Preprints (www.preprints.org) | NOT PEER-REVIEWED | Posted: 23 December 2022 doi:10.20944/preprints202212.0436.v1

2.3. Cell viability in ATCC RAW 264.7 cells

Figures 5a and 5b show the ATCC RAW 264.7 cell viability percentage under different concentrations (3.9-2000 μg·mL^{-1}) of MNPs-Fe (50GS-MNPs, 50MW-MNPs-Fe, and 50CO-MNPs-Fe) for 24 hours and 8 days, respectively.

The percentage of cell viability of ATCC RAW 264.7 cells under concentrations up to 250 μg·mL^{-1} of MNPs-Fe (GS, MW, and CO) did not present significant changes at 24 hours and 8 days. The IC50 (inhibition of 50% of the cells) obtained at 8 days with the samples 50GSMNPs-Fe, 50MW-MNPs-Fe, and 50CO-MNPs-Fe was 461.4 μg·mL^{-1}, 217.7 μg·mL^{-1}, and 520.2 μg·mL^{-1}, respectively. While at 24 hours, IC50 values of 318 μg·mL^{-1}, 1274 μg·mL^{-1}, and 601.6 μg·mL^{-1} were obtained with the 50GSMNPs-Fe, 50MW-MNPs-Fe, and 50CO-MNPs-Fe samples, respectively. IC50 was calculated in GraphPad Prism software with a 95% confidence interval and a four-parameter logistic fit (nonlinear least squares regression).

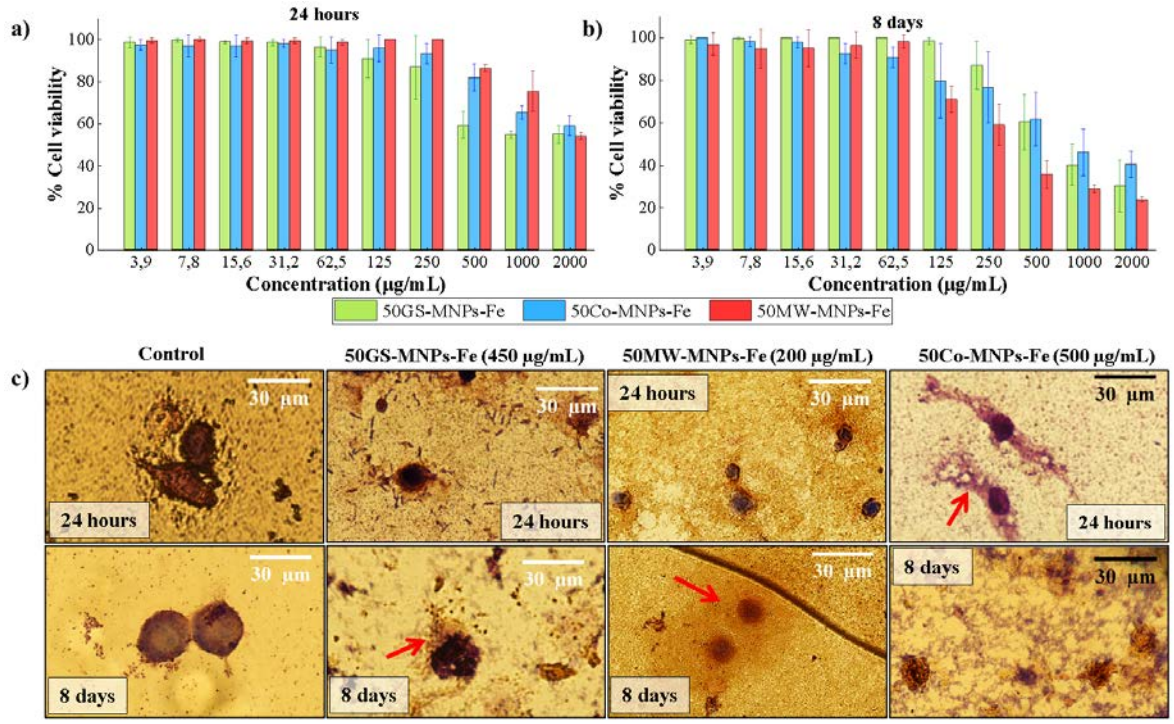

Figure 4. Cell viability percentage in ATCC RAW 264.7 cells by Resazurin cell viability assay, using 50GS-MNPS-Fe, 50MW-MNPS-Fe, and 50CO-MNPS-Fe in 3.9-2000 μg·mL^{-1}concentrations for 24 hours and 8 days, b) Images obtained with Confocal Microscope of ATCC RAW 264.7 cells incubated with 50GS-MNPS-Fe, 50MW-MNPS-Fe, and 50CO-MNPS-Fe to 450 μg·mL^{-1}, 200 μg·mL^{-1}, and 500 μg·mL^{-1}, respectively, at 24 hours and 8 days. All images at 100x magnification.

The cell viability of ATCC RAW 264.7 cells under concentrations up to 250 μg·mL^{-1} of MNPs-Fe (GS, MW, and CO) did not present significant changes (80-100%) at 24 hours. In contrast, after 8 days, the 50MW-MNPs-Fe and 50CO-MNPs-Fe samples did not show significant differences in cell viability (80-100%) for concentrations lower than 62.8 μg·mL^{-1}, while the 50GS-MNPs- Fe was maintained at 250 μg·mL^{-1} (80-100% cell viability). This result is consistent with other studies with low concentrations (100-300 μg·mL^{-1}) of MNPs-Fe (100,101), where negligible cytotoxicity is reported.

These results can be confusing. However, these results can be elucidated by considering the state of the aqueous solutions studied by DLS (see Figure S7). The 50MW-MNPs-Fe samples present more aggregates, followed by the 50CO-MNPs-Fe samples. Therefore, the number of MNPs-Fe dispersed and available for internalization in the ATCC RAW 264.7 cells is reduced, which leads to less cytotoxicity. Thus, in 24 hours, the 50GS-MNPs-Fe samples are apparently more cytotoxic. Still, in reality, we could say that they are better

 doi:10.20944/preprints202212.0436.v1

dispersed with fewer aggregates in such a way that there are more MNPs-Fe internalized in the macrophage cells, causing oxidative stress. After 8 days, the naked 50MW-MNPs-Fe and 50CO-MNPs-Fe samples (without organic coating) degrade as a source of Fe^{+2} and Fe^{+3} ions towards the cell culture medium. These ions are highly reactive and cause oxidative stress and, therefore, more significant cytotoxicity. This result explains the dramatic change in IC50 at 24 hours and 8 days in 50MW-MNPs-Fe. In samples with 50GS-MNPs-Fe, those mentioned above can also occur, but to a lesser extent, that is, the organic coating prevents their aggregation, as observed in DLS Figure S7.

The results suggested that in short periods (24 hours), 50MW-MNPs-Fe and 50CO-MNPs-Fe have lower cytotoxicity. That is, 50% of ATCC RAW 264.7 cells maintained their normal mitochondrial metabolic function at around 1274 and 601.6 $\mu g \cdot mL^{-1}$ concentrations for 50MW-MNPs-Fe and 50CO-MNPs-Fe, respectively. In contrast, the 50GS-MNPs-Fe samples achieved an IC50 of 318.2 $\mu g \cdot mL^{-1}$. That is, a lower concentration of MNPs-Fe caused more significant cell death. In more prolonged periods (8 days), the IC50 induced by the 50GS-MNPs-Fe and 50CO-MNPs-Fe samples were higher (461.4 and 520.2 $\mu g \cdot mL^{-1}$), while the 50MW-MNPs-Fe samples were more cytotoxic. (217.7 $\mu g \cdot mL^{-1}$).

Figure 5c presents images taken with a focal microscope of the Giemsa staining assay, with ATCC RAW 264.7 cells at concentrations of 450 $\mu g \cdot mL^{-1}$, 200 $\mu g \cdot mL^{-1}$, and 500 $\mu g \cdot mL^{-1}$ of 50GS-MNPs-Fe, 50MW-MNPs-Fe, and 50CO-MNPs-Fe, respectively. The concentrations in the Giemsa staining assay were approximate to the IC50 calculated at 8 days in the Resazurin cell viability assay. The Giemsa staining assay enabled to study of the damage and changes produced by MNPs-Fe in ATCC RAW 264.7 cells. At 24 hours, the 50GS-MNPs-Fe sample reduced the size of the ATCC RAW 264.7 cells compared to the control. At 8 days, a cell size like that of the control was observed, as well as a small leak of the cytoplasm (red arrow). At 24 hours and 8 days, chromatin condensation was observed without significant changes in the morphology of the cell membrane, which indicates death by apoptosis. A lack of nutrients or excess ROS can cause this programmed cell death. ROS can induce mitosis death, which arises from removing ROS-overproducing mitochondria by autophagy (102).

In contrast, the samples with 50MW-MNPs-Fe induced a reduction in cell size and significant cytoplasm leakage after 24 hours and 8 days. Likewise, the 50CO-MNPs-Fe samples caused severe damage to the cell membrane and the leakage of the cytoplasmic elements (red arrows). Both types of Fe-MNPs (CO and MW) produced a necrosis-like death, a more aggressive and uncontrolled death.

50GS-MNPs-Fe presents advantages over those obtained by CO and MW in terms of biocompatibility since the organic molecules of the orange peel prevent their aggregation and induce cell death by apoptosis in higher concentrations.

2.4. Photothermal Studies

Figure 6 depicts the photothermal study of aqueous solutions with 50GS-MNPs-Fe, 50MW-MNPs-Fe, and 50CO-MNPs-Fe at concentrations of 8 $mg \cdot mL^{-1}$, including the control sample of DI water. All samples were irradiated under the red light of 630 nm and 65.5 $mW \cdot cm^{-2}$ from an LED source. On the horizontal axis of Figure 6, the doses of light supplied are linked according to the irradiation times (increments of two minutes) with a total of 44 minutes of irradiation. All the MNPs-Fe solutions indicated that the temperature reaches a temperature threshold at 30 minutes. The 50GS-MNPs-Fe, 50MW-MNPs-Fe, and 50CO-MNPs-Fe reached maximum temperatures of 50.8±0.2 °C, 51.7±0.6 °C, and 49.6±0.71 °C, respectively, while the control sample (DI water) reached 42.3±0.1 °C. The photothermal effect was due to this type of nanoparticle LSPR (30). These results indicate that all samples are suitable PATs in the PTT for eliminating bacterial and/or tumor cells (13,42,103).

It is essential to highlight that the 50GS-MNPs-Fe sample achieved a photothermal effect similar to MW and CO, despite having a lower amount of magnetite and maghemite

Preprints (www.preprints.org) | NOT PEER-REVIEWED | Posted: 23 December 2022 doi:10.20944/preprints202212.0436.v1

phase. The concentrations for this study were obtained with the weight obtained after the synthesis.

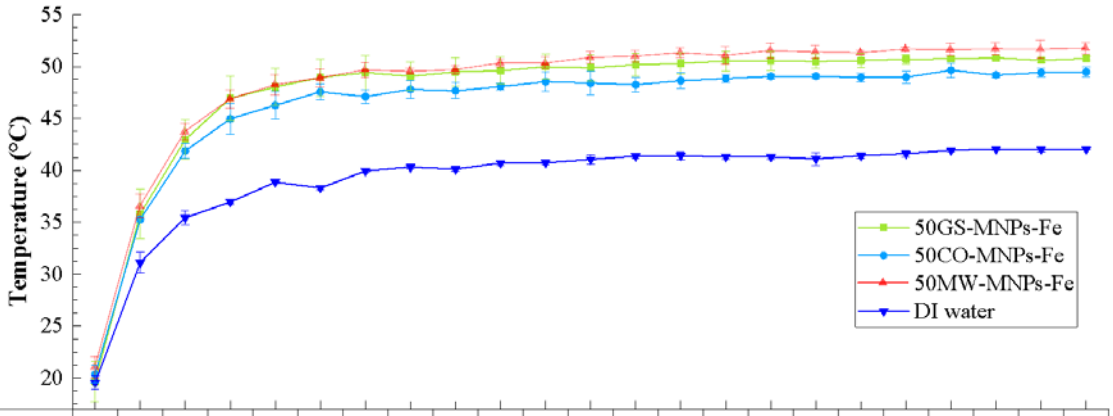

Time (*min*)	0	2	4	6	8	10	12	14	16	18	20	22	24	26	28	30	32	34	36	38	40	42	44
Light dose (J/cm^2)	0,0	7,8	15,7	23,5	31,4	39,3	47,1	55,0	62,8	70,7	78,6	86,4	94,3	102,1	110,0	117,9	125,7	133,6	141,4	149,3	157,2	165,0	172,9

Figure 5. Thermal study of aqueous solutions with 50GS-MNPs-Fe, 50MW-MNPs-Fe, and 50CO-MNPs-Fe at concentrations of 8 mg·mL^{-1} and the control sample of DI water with red light irradiation at 630 nm and 65.5 mW·cm^{-2} from an LED source.

2.5. Antibacterial PTT

Figures 7a-b show the Log$_{10}$ (CFU) count of the spread plate assays in *S. Aureus* and *E. Coli* bacteria, respectively. All groups were treated with MNPs-Fe (GS, MW, and CO) using a concentration of 8 mg·mL^{-1} of MNPs-Fe in PBS. The antibacterial activity of 50GS-MNPs-Fe against *S. Aureus* without irradiation is small in 0.25 Log$_{10}$ (CFU). Likewise, 50MW-MNPs-Fe and 50CO-MNPs-Fe without irradiation did not have significant antibacterial activity. Irradiation with a red light at 630 nm (65.5 mW·cm^{-2}) for 30 minutes towards *S. Aureus* (without MNPs-Fe) had no antibacterial effect. However, 50GS-MNPs-Fe and 50CO-MNPs-Fe with red light irradiation at 630 nm (65.5 mW·cm^{-2}) for 30 minutes completely inhibited *S. Aureus* bacteria. The 50MW-MNPs-Fe with red light irradiation at 630 nm (65.5 mW·cm^{-2}, 30 min) inhibited 3.99 Log (CFU) of *S. Aureus*.

Preprints (www.preprints.org) | NOT PEER-REVIEWED | Posted: 23 December 2022 doi:10.20944/preprints202212.0436.v1

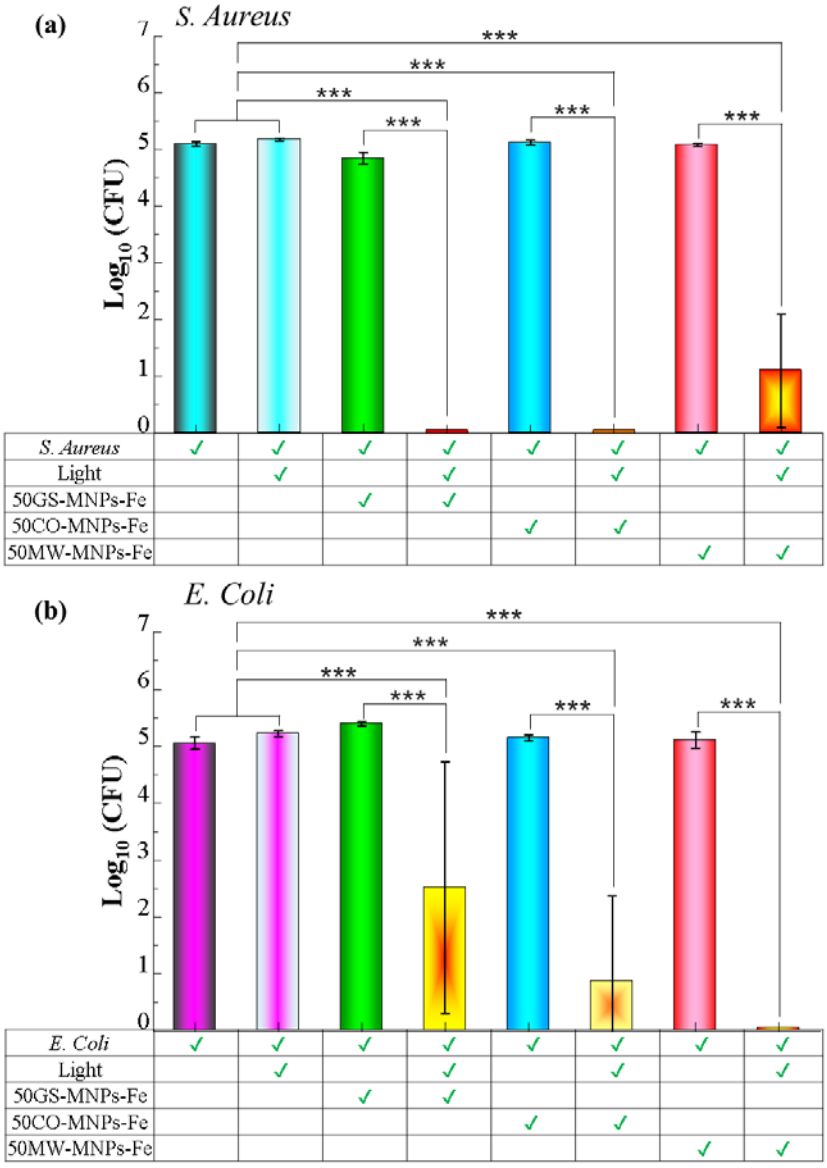

Figure 6. Counting of Log_{10} (CFU) in the spread plate assay to groups; [Bacteria], [Bacteria + Light], [Bacteria + MNPs-Fe (GS, MW, CO)], and [Bacteria + MNPs-Fe (GS, MW, CO) + light], in a) *S. Aureus* y b) *E. Coli*. Significant differences in means according to the Tukey test (*** $p \leq 0{,}001$).

The antibacterial activity of all MNPs-Fe (GS, MW, and CO) against *E. Coli* is negligible. The 50MW-MNPs-Fe irradiated with a red light at 630 nm (65.5 $mW \cdot cm^{-2}$, 30 min) completely inhibited *E. Coli*, while the 50GS-MNPs-Fe and 50CO-MNPs-Fe were able to inhibit 2.54 Log_{10} (CFU) and 4.19 Log_{10} (CFU), respectively. The results indicated that 50GS-MNPs-Fe and 50CO-MNPs-Fe have excellent antibacterial activity against *S. Aureus* (gram-positive), see Figure 8a, while 50MW-MNPs-Fe are capable of inhibiting gram-bacteria negative as *E. Coli*.

The photothermal effect of the MNPs-Fe produces bacterial elimination. Figure 8b shows that the final temperature after the irradiation (antibacterial PTT) was higher than 50 °C for both bacterial strains, while the controls of light (Bacteria + light) reached temperatures around 40 °C. In all the irradiated cases, the dose of light supplied corresponds to 117.9 $J \cdot cm^{-2}$.

Preprints (www.preprints.org) | NOT PEER-REVIEWED | Posted: 23 December 2022 doi:10.20944/preprints202212.0436.v1

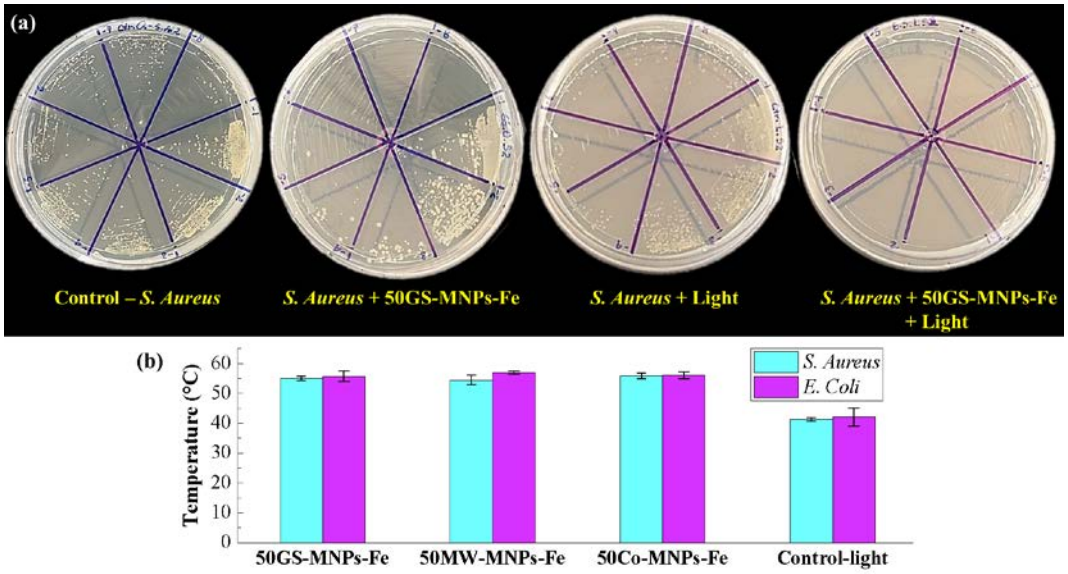

Figure 7. a) Images of the spread plate assay of the groups: [S. aureus], [S. Aureus + light], [S. Aureus + 50GS-MNPs-Fe], [S. Aureus + 50GS-MNPs-Fe + Light], b) Temperatures reached in antibacterial PTT after irradiation with 117.9 J·cm^{-2}.

The results of the antibacterial activity indicate that the 50GS-MNPs-Fe inhibit *S. Aureus* and partially *E. Coli*, which is in accordance with (78). However, the concentrations of MNPs-Fe used in our studies are higher, reaching temperatures of ~ 50°C in antibacterial PTT, like those reported by Qing G. *et al*. (104) from 43-49 °C (with 808 nm, 0.5 W·cm^{-2}).

3. Materials and Methods

3.1. Materials

Iron III chloride hexahydrate ($FeCl_3 \cdot 6H_2O$) from Mallinckrodt Chemical Ltd. Iron II sulfate heptahydrate ($FeSO_4 \cdot 7H_2O$) from MERCK. Ammonium hydroxide (NH_4OH) from BDH chemicals. DMEM-Dulbecco's Modified Eagle Medium from Gibco. Resazurin sodium salt from Sigma Aldrich. Difco Mueller Hinton Broth and Difco Mueller Hinton Agar from Becton and Dickinson. No further purification was performed on the chemical agents.

3.2. Preparation of orange peel extract

First, the endocarp and inner mesocarp were removed from the orange waste to obtain only the orange peel (outer mesocarp). Then, small pieces approximately 1x2 cm in size were obtained. 25 g of orange peel was weighed and thoroughly washed using deionized (DI) water. The orange peel and 250 mL of DI water were blended using a domestic blender at 2000 rpm for 10 minutes (Oster-4172, 375 W). The mixture was irradiated in a domestic MW oven (General Electric, JES-700 W) for 5 minutes. Finally, the mixture was cooled and sieved using paper filters (Brew Rite). The vegetal extract was used within the next 30 minutes.

3.3. GS of MNPs-Fe

$FeCl_3 \cdot 6H_2O$ (210 mg) and $FeSO_4 \cdot 7\ H_2O$ (105 mg) were dissolved in 10 mL DI water in a beaker at 70 °C with continuous magnetic stirring. Then several mixtures of 25 mL of orange peel extract with NH_4OH were prepared in different volume percentages: 100%, 75%, 50%, 25%, and 0% NH_4OH. A solution of $FeCl_3 \cdot 6H_2O$ and $FeSO_4 \cdot 7H_2O$ was added to each mixture of orange peel extract and NH_4OH and subsequently irradiated with MW (General Electric, JES-70W) for three intervals of 30 seconds. The black appearance indicated the formation MNPs-Fe, which were washed with DI water and under a magnetic field to remove phytochemicals excess and non-magnetic particles. The MNPs-Fe

 doi:10.20944/preprints202212.0436.v1

obtained with 100%, 75%, 50%, 25%, and 0% of NH_4OH are called as 100GS-MNPs-Fe, 75GS-MNPs-Fe, 50GS-MNPs-Fe, 25GS-MNPs-Fe, and 0GS-MNPs-Fe respectively.

To compare the weight yield of the GS, cytotoxicity, antibacterial activity, and magnetic properties such as saturation magnetization (Ms) and blocking temperature (T_B), MNPs-Fe were prepared by CO and MW route without peel orange extract. In the case of CO synthesis, a procedure similar to that described in (63,64) was followed, using $FeCl_3 \cdot 6H_2O$ (210 mg) and $FeSO_4 \cdot 7\ H_2O$ (105 mg) as precursors with the identical aliquots used in GS. Mixtures according to the percentages used in the GS were prepared with DI water and NH_4OH. Then the temperature was raised to 80 °C in a hot plate. Later, the solution of precursor salts was added drop by drop. Magnetic stirring was maintained for 1 hour, and then the nanoparticles were washed with DI water and a permanent magnet. The MW synthesis followed the same procedure as the GS (24,65), replacing the orange peel extract with DI water. The samples obtained by CO with 100%, 75%, 50%, and 25 % of NH_4OH (volume) were called as 100CO-MNPs-Fe, 75CO-MNPs-Fe, 50CO-MNPs-Fe, and 25CO-MNPs-Fe, respectively. The samples obtained by MW synthesis were denominated as 100MW-MNPs-Fe, 75MW-MNPs-Fe, 50MW-MNPs-Fe, and 25MW-MNPs-Fe, according to the percentage of NH_4OH used.

In the different tests, samples of MNPs-Fe were in aqueous dispersions and powder (dry). In the case of MNPs-Fe powder, drying was carried out in an oven at 40 °C for 42 hours.

3.4. MNPs-Fe characterization

The morphology and size distribution of the MNPs-Fe were studied by Scanning Electron Microscopy (SEM) in a Tescan Mira 3 microscope equipped with a Schottky field emission source at 25 kV. For this, an aliquot of MNPs-Fe was dispersed in 1 mL of DI water and then dried on a sample holder at room temperature. To measure the hydrodynamic diameter of the MNPs-Fe, a Dynamic Light Scattering (DLS) analysis was performed in a Particle Size Analyzer 90Plus-11554 (Brookhaven Instruments Corporation). Thus, 5 mL of dispersion was used for the sample of MNPs-Fe in DI water at 1 $mg \cdot mL^{-1}$. The topography of MNPs-Fe was studied by Atomic Force Microscopy (AFM) in a Dimension Icon Atomic Force Microscope (Bruker), in Tapping Mode with a scanning range of 90 μm x 90 μm (XY) and 10 μm (Z) equipped with a Dim 4000 type scanner. An aliquot of MNPs-Fe on DI water was used at 10 mg·mL-1.

The elemental composition was determined by Energy Dispersive X-ray Spectroscopy (EDS) in the same Tescan Mira 3 microscope using a detector Xflash ® 6-30, Bruker, with a resolution of 123 eV in Mn Kα. The crystalline structure and phases of iron oxide in the MNPs-Fe were identified by X-ray Diffraction (XRD) in an Empyrean diffractometer (Malvern Panalytical) equipped with a copper X-ray tube (Empyrean Cu LFF) and Cu-Kα radiation at 2θ=5°-90° with 45 kV and 40 mA. For this, 93.3-434 mg of MNPs-Fe powder was used. Fourier transform infrared (FTIR) and Raman spectroscopy allowed the study of the molecular vibrations of MNPs-Fe. FTIR spectra were acquired using a Spectrum 100 (86660) spectrometer (Perkin Elmer) equipped with a Spotlight 200 N/S 86672 microscope with an analysis range of 500-4000 cm^{-1} and 5 mg of MNPs-Fe powder. Raman spectra were recorded using a LabRAM HR Evolution spectrometer (HORIBA Corporation) with an analysis range between 100-2000 cm^{-1} and a sensitivity of 10 cm^{-1}. For this, 5 mg of MNPs-Fe were dispersed in 5 mL of DI water, and an aliquot was dried on a glass slide at room temperature.

The magnetic behavior of MNPs-Fe was analyzed in a Quantum Design Versalab Vibrating Sample Magnetometer (VSM) (Quantum Design) with an operating range of -3 to 3 Tesla (-30 kOe a 30 kOe) and 50-400 K with sensitivity ~ $1x10^{-6}$ emu. Thus, generated two types of curves: magnetization (M) as a function of the external magnetic field (H) at a constant temperature and magnetization (M) as a function of temperature (cooling from 315 K to 60 K) in the presence of zero magnetic fields (zero field cooling, ZFC curves) and with the presence of a small magnetic field 50 Oe (field cooling, FC curves).

Preprints (www.preprints.org) | NOT PEER-REVIEWED | Posted: 23 December 2022 doi:10.20944/preprints202212.0436.v1

3.5. Cytotoxicity assay

Cytotoxicity assays measure the rate of proliferation and the toxic effects on the cell when using certain materials, such as MNPs-Fe. Particularly, this cytotoxicity study used as a test subject, an animal cell line ATCC RAW 264.7 of the macrophage type from mice (Mus musculus), donated by CISeAL.

3.5.1. Cell culture

The animal cell line ATCC RAW 264.7 remained in DMEM-Dulbecco's Modified Eagle Medium accompaniment with 1% penicillin/streptomycin and fetal bovine serum (FBS) – 10% (DMEM-10) in a Series II Water Jacket – CO_2 Incubator-Thermo Scientific, at 37 °C in an atmosphere of CO_2 5% and 98% relative humidity (RH) for 24 hours.

3.5.2. Resazurin cell viability assay

Within a 96-well plate with a black background, $2x10^4$ cells/well were seeded using 100 µL of DMEM-10 (incubated at 37 °C) with an atmosphere of 5% CO_2 and 98% of RH for 24 hours. MNPs-Fe were diluted in 10-fold serial dilutions (2000, 1000, 500, 250, 125, 62.5, 31.2, 15.6, 7.8, 3.9 $\mu g \cdot mL^{-1}$) with DMEM-10. They were then placed in the seeded cells, maintaining the respective life control wells. Thus, 10 µL of resazurin sodium salt at 3 mM in PBS per well was added, and the plate was incubated for 24 hours. Finally, fluorescence was measured at 520, 580, and 640 nm excitation on a GloMax (Promega) multimodal microplate reader. In viable cells with adequate mitochondrial metabolic function, redox reactions occurred between the mitochondrial coenzymes nicotinamide adenine dinucleotide NADH (reduced form) and its oxidized NAD^+, irreversibly reducing resazurin to resorufin. The resorufin fluoresces at 560 nm, then excrete it to the culture medium, where it was quantified with a plate fluorometer, this signal being a function of the number of viable cells in the sample (66,67).

3.5.3. Giemsa staining assay

Three sterile circular coverslips per well were aseptically placed into two 6-well plates, and $5.5x10^5$ ATCC RAW 264.7 cells per well were plated and incubated at 37 °C with a 5% CO_2 atmosphere and 98% HR. The following day, cells were washed with PBS, and the MNPs-Fe were added and incubated. A coverslip was removed from each well at 24 hours and 8 days, later fixed with 5% of glutaraldehyde for 24 hours, and later immersed in Giemsa stain for 30 minutes. Finally, images were taken with a confocal microscope. This assay was carried out to stain the cell organelles and observe the damage caused by the presence of MNPs-Fe, such as cytoplasmic condensations, damage to the cell membrane, and so on.

3.6. Antibacterial activity

Antibacterial activity studies used *S. Aureus* ATCC 25923 and *E. Coli* ATCC 25922 bacteria as test subjects (both donated by CISeAL). Light irradiation-assisted PTT was employed as an antibacterial strategy, which converts light energy into heat that kills bacterial cells by rising local temperature.

3.6.1. Thermal studies

The photothermal studies measured the temperature increase with a digital thermometer DET-306 (SCANMED, 0.1 °C sensitivity) in MNPs-Fe solutions and DI water at 8 $mg \cdot mL^{-1}$ with red light irradiation of 630 nm from a 65.5 $mW \cdot cm^{-2}$ LED source. The temperature was registered every two minutes until its increase stopped.

3.6.2. Bacterial culture

For bacterial culture, cryovials were provided with *S. Aureus* and *E. Coli* bacteria that were thawed at room temperature and inoculated in Muller Hinton Broth (Difco™) for

 doi:10.20944/preprints202212.0436.v1

incubation (SL Shel lab incubator – 1525) for 24 hours at 37 °C. The number of Colonies Forming Units (CFU) was established using a spectrophotometer (Thermo Scientific ™ Orion™ AquaMate 8000 UV-Vis) for absorbance of 0.2 OD and 0.4 OD, equivalent to 10^7 CFU·mL^{-1} for *E. Coli* and 10^6 CFU·mL^{-1} for *S. Aureus,* respectively.

3.6.3. Spread plate assay

Four groups were considered for each bacterium: (1) control (bacteria alone), (2) bacterium + light, (3) bacterium + MNPs-Fe, and (4) bacterium + MNPs-Fe + light. All assays were performed in triplicate. Consequently, 1 mL of bacterial culture (*E. Coli* and *S. Aureus*) was taken and centrifuged at 3000 rpm for 10 minutes. Then, the supernatant was discarded, and 1 mL of MNPs-Fe dispersed in PBS was added (8 mg·mL^{-1}) or PBS according to the test groups and homogenized with vortex. Each sample was incubated in the dark for 25 minutes at 37 °C. Then, bacteria + light and bacteria + MNPs-Fe + light groups were irradiated with red light (630 nm) in a LED source of 65.5 mW·cm^{-2} for 30 minutes. Later, an aliquot of 0.5 mL of each sample was taken to eight serial dilutions (1:2 to 1:256) in PBS to inoculate 4 µL of each dilution into a divided eight-parts Petri dish with Muller Hinton Agar (Difco ™) spread. Finally, the Petri dishes were incubated at 37 °C for 24 hours to count the CFU.

4. Conclusion

In this work, orange peel residues from local commerce were employed to synthesize MNPs-Fe by an environmentally friendly approach. The as-synthesized nanomaterials were characterized by morphological, topographic, structural, and magnetic studies and vibrational analysis of molecules. The results allowed us to identify nano-spheres with crystalline structures of magnetite and maghemite phases. Besides, a SPM behavior and a crown of organic molecules on the surface of MNPs-Fe (from the orange peel) were identified. The synthesis of several MNPs-Fe through GS, CO, and MW allowed us to study the influence of NH_4OH on the weights of MNPs-Fe to select the minimum aliquot of NH_4OH to maintain an adequate weight yield of GS, being 50% v/v. Photothermal studies indicated that 50GS-MNPs-Fe reached a photothermal effect similar to those obtained by MW and CO (~ 50°C), indicating that the organic molecules did not affect light conversion into heat. Cytotoxicity studies reflected low toxicity of all the MNPs-Fe for concentrations lower than 250 ug/mL, with an improvement in the viability of the macrophages at 8 days with 50GS-MNPs-Fe. Likewise, the 50GS-MNPs-Fe sample inhibited *S. Aureus*, but not wholly *E. Coli*, because gram-negative bacteria have a robust bacterial wall structure (lipopolysaccharides, peptidoglycan, and phospholipids). We also found a SPM behavior of 50GS-MNPs-Fe above 60 K. These results indicate that 50GS-MNPs-Fe are suitable candidates as broad-spectrum PTAs in antibacterial PTT, MRI, and magnetic hyperthermia since they have terpenes and a SPM behavior.

Conflicts of Interest: The authors declare that the research was conducted without any commercial or financial relationships that could be construed as a potential conflict of interest.

Author Contributions: All authors agree to be accountable for the content of the work.

Funding: Project PIIF-20-05. National Polytechnic School.

References

1. Wang L, Hu C. The antimicrobial activity of nanoparticles : present situation and prospects for the future. 2017;1227–49.
2. Kong X, Liu X, Zheng Y, Chu PK, Zhang Y, Wu S. Graphitic carbon nitride-based materials for photocatalytic antibacterial application. Mater Sci Eng R Reports. 2021;145(March):100610.
3. Liang J, Li W, Chen J, Huang X, Liu Y, Zhang X, et al. Antibacterial Activity and Synergetic Mechanism of Carbon Dots against Gram-Positive and -Negative Bacteria. ACS Appl Bio Mater. 2021;4(9):6937–45.
4. Rodrigues GR, López-abarrategui C, De I, Gómez S. Antimicrobial magnetic nanoparticles based-therapies for controlling infectious diseases . Int J Pharm. 2018;
5. Paramanantham P, Anju VT, Dyavaiah M, Siddhardha B. Applications of Carbon-Based Nanomaterials for Antimicrobial Photodynamic Therapy. In: Nanotechnology in the Life Sciences. 2019. p. 237–59.

6. Feng Y, Liu L, Zhang J, Aslan H, Dong M. Photoactive antimicrobial nanomaterials. J Mater Chem B. 2017;5(44):8631–52.
7. Smith M. Antibiotic Resistance Mechanisms. Journeys Med Res Three Cont Over 50 Years. 2017;(May 2017):95–9.
8. El-Gendy NS, El-Gendy NS, Omran BA. Green Synthesis of Nanoparticles for Water Treatment. Nano Bio-Based Technol Wastewater Treat. 2019;205–63.
9. Ajinkya N, Yu X, Kaithal P, Luo H, Somani P. Magnetic Iron Oxide Nanoparticle (IONP) Synthesis to Applications : Present and Future. 2020;1–35.
10. Xin Q, Shah H, Nawaz A, Xie W, Akram MZ, Batool A, et al. Antibacterial Carbon-Based Nanomaterials. Adv Mater. 2019;31(45):1–15.
11. Jalal M, Ansari MA, Alzohairy MA, Ali SG, Khan HM, Almatroudi A, et al. Biosynthesis of silver nanoparticles from oropharyngeal candida glabrata isolates and their antimicrobial activity against clinical strains of bacteria and fungi. Nanomaterials. 2018;8(8).
12. Journal OA. Biointerface Research in Applied Chemistry. 2020;10(4):5951–9.
13. Jabir MS, Nayef UM, Kadhim WKA. Polyethylene glycol-functionalized magnetic (Fe3O4) nanoparticles: A novel DNA-mediated antibacterial agent. Nano Biomed Eng. 2019;11(1):18–27.
14. Rumyantceva V, Rumyantceva V, Koshel E, Vinogradov V. Biocide-conjugated magnetite nanoparticles as an advanced platform for biofilm treatment. Ther Deliv. 2019;10(4):241–50.
15. Ling W, Wang M, Xiong C, Xie D, Chen Q, Chu X, et al. Synthesis , surface modi fi cation , and applications of magnetic iron oxide nanoparticles. 2019;
16. Chen Y, Gao Y, Chen Y, Liu L, Mo A, Peng Q. Nanomaterials-based photothermal therapy and its potentials in antibacterial treatment. J Control Release [Internet]. 2020;328(September):251–62. Available from: https://doi.org/10.1016/j.jconrel.2020.08.055
17. Jędrzak A, Grześkowiak BF, Golba K, Coy E, Synoradzki K, Jurga S, et al. Magnetite nanoparticles and spheres for chemo-and photothermal therapy of hepatocellular carcinoma in vitro. Int J Nanomedicine. 2020;15:7923–36.
18. Songca SP, Adjei Y. Applications of Antimicrobial Photodynamic Therapy against Bacterial Biofilms. Vol. 23, International Journal of Molecular Sciences. 2022. p. 3209.
19. Noval VE, Puentes CO, Carriazo JG. Magnetita (Fe3O4): Uma estrutura inorgânica com múltiplas aplicações em catálise heterogénea. Rev Colomb Quim. 2017;46(1):42–59.
20. Frey PA, Reed GH. The ubiquity of iron. ACS Chem Biol. 2012;7(9):1477–81.
21. Wang WW, Zhu YJ, Ruan ML. Microwave-assisted synthesis and magnetic property of magnetite and hematite nanoparticles. J Nanoparticle Res. 2007;9(3):419–26.
22. Luz M, Pisciotti M. ESTUDIO DEL PROCESO DE CALENTAMIENTO DE NANOPART´ICULAS MAGN´ETICAS CON CAMPOS MAGN´ETICOS AC PARA SU UTILIZACI´ON EN TRATAMIENTO DE TUMORES POR HIPERTERMIA. 2009;
23. Mackintosh D. Seismic Traveltime Tomography. Sugar Milling. 2001;I(March 2019):311–8.
24. Bano S, Nazir S, Nazir A, Munir S, Mahmood T, Afzal M, et al. Microwave-assisted green synthesis of superparamagnetic nanoparticles using fruit peel extracts: Surface engineering, T2relaxometry, and photodynamic treatment potential. Int J Nanomedicine. 2016;11:3833–48.
25. Orna Sánchez. Universidad Nacional Mayor de San Marcos. Medicina (B Aires). 2013;447(May):1–33.
26. Bobo D, Robinson KJ, Islam J, Thurecht KJ, Corrie SR. Nanoparticle-Based Medicines: A Review of FDA-Approved Materials and Clinical Trials to Date. Pharm Res. 2016;33(10):2373–87.
27. Martinelli C, Pucci C, Ciofani G. Nanostructured carriers as innovative tools for cancer diagnosis and therapy. APL Bioeng. 2019;3(1).
28. Wiart M, Tavakoli C, Hubert V, Hristovska I, Dumot C, Parola S, et al. Use of metal-based contrast agents for in vivo MR and CT imaging of phagocytic cells in neurological pathologies. J Neurosci Methods. 2023;383.
29. Hu T, Wang Z, Shen W, Liang R, Yan D, Wei M. Recent advances in innovative strategies for enhanced cancer photodynamic therapy. Theranostics. 2021;11(7):3278–300.
30. Estelrich J, Antònia Busquets M. Iron oxide nanoparticles in photothermal therapy. Molecules. 2018;23(7).
31. Hu M, Chen J, Li ZY, Au L, Hartland G V., Li X, et al. Gold nanostructures: Engineering their plasmonic properties for biomedical applications. Chem Soc Rev. 2006;35(11):1084–94.
32. Patil RM, Thorat ND, Shete PB, Bedge PA. Comprehensive cytotoxicity studies of superparamagnetic iron oxide nanoparticles. Biochem Biophys Reports. 2018;13(December 2017):63–72.
33. Peng Y, Xia C, Cui M, Yao Z, Yi X. Effect of reaction condition on microstructure and properties of (NiCuZn)Fe2O4 nanoparticles synthesized via co-precipitation with ultrasonic irradiation. Ultrason Sonochem. 2021;71:105369.
34. Liu Y, Guo Z, Li F, Xiao Y, Zhang Y, Bu T, et al. Multifunctional Magnetic Copper Ferrite Nanoparticles as Fenton-like Reaction and Near-Infrared Photothermal Agents for Synergetic Antibacterial Therapy. ACS Appl Mater Interfaces. 2019;11(35):31649–60.
35. Nel AE, Mädler L, Velegol D, Xia T, Hoek EMV, Somasundaran P, et al. Understanding biophysicochemical interactions at the nano-bio interface. Nat Mater. 2009;8(7):543–57.
36. Sharma SK. Complex magnetic nanostructures: Synthesis, assembly and applications. Complex Magnetic Nanostructures: Synthesis, Assembly and Applications. 2017. 1–464 p.
37. Chen BW, He YC, Sung SY, Le TTH, Hsieh CL, Chen JY, et al. Synthesis and characterization of magnetic nanoparticles coated with polystyrene sulfonic acid for biomedical applications. Sci Technol Adv Mater. 2020;21(1):471–81.

38. Cordeiro AP, Feuser PE, Araújo PHH, Sayer C. Encapsulation of Magnetic Nanoparticles and Copaíba Oil in Poly(methyl methacrylate) Nanoparticles via Miniemulsion Polymerization for Biomedical Application. Macromol Symp. 2020;394(1):1–5.
39. Hussain SM, Hess KL, Gearhart JM, Geiss KT, Schlager JJ. In vitro toxicity of nanoparticles in BRL 3A rat liver cells. Toxicol Vitr. 2005;19(7):975–83.
40. Tousi MS, Sepehri H, Khoee S, Farimani MM, Delphi L, Mansourizadeh F. Evaluation of apoptotic effects of mPEG-b-PLGA coated iron oxide nanoparticles as a eupatorin carrier on DU-145 and LNCaP human prostate cancer cell lines. J Pharm Anal. 2021;11(1):108–21.
41. Alarifi S, Ali D, Alkahtani S. Iron Oxide Nanoparticles Induce Oxidative Stress , DNA Damage , and Caspase Activation in the Human Breast Cancer Cell Line. 2014;
42. E CC, Carolina N. Relation between the Redox State of Iron-Based Nanoparticles and Their Cytotoxicity toward Escherichia coli. 2008;42(17):6730–5.
43. Wei H, Hu Y, Wang J, Gao X, Qian X, Tang M. Superparamagnetic iron oxide nanoparticles: Cytotoxicity, metabolism, and cellular behavior in biomedicine applications. Int J Nanomedicine. 2021;16(May):6097–113.
44. Ijaz I, Gilani E, Nazir A, Bukhari A. Detail review on chemical, physical and green synthesis, classification, characterizations and applications of nanoparticles. Green Chem Lett Rev. 2020;13(3):59–81.
45. Hezam FA, Khalifa NO, Nur O, Mustafa MA. Synthesis and magnetic properties of Ni0.5MgxZn0.5-xFe2O4 ($0.0 \leq x \leq 0.5$) nanocrystalline spinel ferrites. Mater Chem Phys. 2021;257(September 2020):123770.
46. Dumani DS, Cook JR, Kubelick KP, Luci JJ, Emelianov SY. Photomagnetic Prussian blue nanocubes: Synthesis, characterization, and biomedical applications. Nanomedicine Nanotechnology, Biol Med. 2020;24:102138.
47. Amiri M, Gholami T, Amiri O, Pardakhti A, Ahmadi M, Akbari A, et al. The magnetic inorganic-organic nanocomposite based on ZnFe2O4-Imatinib-liposome for biomedical applications, in vivo and in vitro study. J Alloys Compd. 2020;849:156604.
48. Escobar AM, Pizzio LR, P. Romanelli G. Catalizadores Magnéticos Basados En Óxidos De Hierro: Síntesis, Propiedades Y Aplicaciones. Cienc En Desarro. 2018;10(1).
49. Novoselova LY. Nanoscale magnetite: New synthesis approach, structure and properties. Appl Surf Sci. 2021;539:148275.
50. Shah Saqib AN, Thu Huong NT, Kim SW, Jung MH, Lee YH. Structural and magnetic properties of highly Fe-doped ZnO nanoparticles synthesized by one-step solution plasma process. J Alloys Compd. 2021;853:157153.
51. Nikolova MP, Chavali MS. Metal oxide nanoparticles as biomedical materials. Biomimetics. 2020;5(2).
52. Maheswari KC, Reddy. Green Synthesis of Magnetite Nanoparticles through Leaf Extract of Azadirachta indica. Jacs Dir. 2016;2(4):189–91.
53. Venkateswarlu S, Rao YS, Balaji T, Prathima B, Jyothi NVV. Biogenic synthesis of Fe3O4 magnetic nanoparticles using plantain peel extract. Mater Lett. 2013;100:241–4.
54. Šuljagić M, Vulić P, Jeremić D, Pavlović V, Filipović S, Kilanski L, et al. The influence of the starch coating on the magnetic properties of nanosized cobalt ferrites obtained by different synthetic methods. Mater Res Bull. 2021;134(October).
55. Kumar I, Mondal M, Sakthivel N. Green synthesis of phytogenic nanoparticles. Green Synthesis, Characterization and Applications of Nanoparticles. Elsevier Inc.; 2019. 37–73 p.
56. Nasrollahzadeh M, Atarod M, Sajjadi M, Sajadi SM, Issaabadi Z. Plant-Mediated Green Synthesis of Nanostructures: Mechanisms, Characterization, and Applications. 1st ed. Vol. 28, Interface Science and Technology. Elsevier Ltd.; 2019. 199–322 p.
57. Singh J, Dutta T, Kim KH, Rawat M, Samddar P, Kumar P. "Green" synthesis of metals and their oxide nanoparticles: Applications for environmental remediation. J Nanobiotechnology. 2018;16(1):1–24.
58. Dhar PK, Saha P, Hasan MK, Amin MK, Haque MR. Green synthesis of magnetite nanoparticles using Lathyrus sativus peel extract and evaluation of their catalytic activity. Clean Eng Technol. 2021;3:100117.
59. Silvestri C, Silvestri L, Forcina A, Di Bona G, Falcone D. Green chemistry contribution towards more equitable global sustainability and greater circular economy: A systematic literature review. J Clean Prod. 2021;294:126137.
60. Nüchter M, Müller U, Ondruschka B, Tied A, Lautenschläger W. Microwave-assisted chemical reactions. Chem Eng Technol. 2003;26(12):1207–16.
61. Henam SD, Ahmad F, Shah MA, Parveen S, Wani AH. Microwave synthesis of nanoparticles and their antifungal activities. Spectrochim Acta - Part A Mol Biomol Spectrosc. 2019;213:337–41.
62. Lazaratos M, Karathanou K, Mainas E, Chatzigoulas A, Pippa N, Demetzos C, et al. Coating of magnetic nanoparticles affects their interactions with model cell membranes. Biochim Biophys Acta - Gen Subj. 2020;1864(11):129671.
63. Mascolo MC, Pei Y, Ring TA. Room Temperature Co-Precipitation Synthesis of Magnetite Nanoparticles in a Large ph Window with Different Bases. Materials (Basel). 2013;6(12):5549–67.
64. Hussein-Al-Ali SH, El Zowalaty ME, Hussein MZ, Geilich BM, Webster TJ. Synthesis, characterization, and antimicrobial activity of an ampicillin-conjugated magnetic nanoantibiotic for medical applications. Int J Nanomedicine. 2014;9(1):3801–14.
65. Zheng B, Zhang M, Xiao D, Jin Y, Choi MMF. Fast microwave synthesis of Fe 3O 4 and Fe 3O 4/Ag magnetic nanoparticles using Fe 2+ as precursor. Inorg Mater. 2010;46(10):1106–11.
66. Number P, Information P, Specification T, Information S, Information T. Product Information Product Information. Opadry. 1920;(14998):1919–20.
67. Bioarray C. Resazurin Cell Viability Assay.
68. López-Téllez G, Balderas-Hernández P, Barrera-Díaz CE, Vilchis-Nestor AR, Roa-Morales G, Bilyeu B. Green method to form iron oxide nanorods in orange peels for chromium(VI) reduction. J Nanosci Nanotechnol. 2013;13(3):2354–61.

69. Kahrilas GA, Wally LM, Fredrick SJ, Hiskey M, Prieto AL, Owens JE. Microwave-Assisted Green Synthesis of Silver Nanoparticles Using Orange Peel Extract. 2013;
70. Petcharoen K, Sirivat A. Synthesis and characterization of magnetite nanoparticles via the chemical co-precipitation method. Mater Sci Eng B Solid-State Mater Adv Technol. 2012;177(5):421–7.
71. Saxena N, Singh M. Efficient synthesis of superparamagnetic magnetite nanoparticles under air for biomedical applications. J Magn Magn Mater. 2017;429:166–76.
72. Rahmayanti M. Synthesis of Magnetite Nanoparticles Using The Reverse Co-precipitation Method With NH4OH as Precipitating Agent and Its Stability Test at Various pH. Nat Sci J Sci Technol. 2020;9(3):54–8.
73. Wroblewski C, Volford T, Martos B, Samoluk J, Martos P. High yield synthesis and application of magnetite nanoparticles (Fe3 o4). Magnetochemistry. 2020;6(2):1–14.
74. Nnadozie EC, Ajibade PA. Green synthesis and characterization of magnetite (Fe3O4) nanoparticles using Chromolaena odorata root extract for smart nanocomposite. Mater Lett. 2020;263:127145.
75. Raja PM V, Barron AR. Physical methods in chemistry. Nature. 2019;134(3384):366–7.
76. Marrese M, Guarino V, Ambrosio L. Atomic Force Microscopy: A Powerful Tool to Address Scaffold Design in Tissue Engineering. J Funct Biomater. 2017;8(1):7.
77. Christensen M, Rasmussen JT, Simonsen AC. Roughness analysis of single nanoparticles applied to atomic force microscopy images of hydrated casein micelles. Food Hydrocoll. 2015;45:168–74.
78. Taimoory SM, Rahdar A, Aliahmad M, Sadeghfar F, Hajinezhad MR, Jahantigh M, et al. The synthesis and characterization of a magnetite nanoparticle with potent antibacterial activity and low mammalian toxicity. J Mol Liq. 2018;265(2017):96–104.
79. Silva VAJ, Andrade PL, Silva MPC, Bustamante AD, De Los Santos Valladares L, Albino Aguiar J. Synthesis and characterization of Fe3O4 nanoparticles coated with fucan polysaccharides. J Magn Magn Mater. 2013;343:138–43.
80. Tomul F, Arslan Y, Başoğlu FT, Babuçcuoğlu Y, Tran HN. Efficient removal of anti-inflammatory from solution by Fe-containing activated carbon: Adsorption kinetics, isotherms, and thermodynamics. J Environ Manage. 2019;238(May):296–306.
81. Akram MA, Khan BA, Khan MK, Alqahtani A, Alshahrani SM, Hosny KM. Fabrication and characterization of polymeric pharmaceutical emulgel co-loaded with eugenol and linalool for the treatment of trichophyton rubrum infections. Vol. 13, Polymers. 2021.
82. Zhang M, Kamavaram V, Reddy RG. New Electrolytes for Aluminum Production: Ionic Liquids. Jom. 2003;55(11):54–7.
83. Khalil OM, Mingareev I, Bonhoff T, El-Sherif AF, Richardson MC, Harith MA. Studying the effect of zeolite inclusion in aluminum alloy on measurement of its surface hardness using laser-induced breakdown spectroscopy technique. Opt Eng. 2014;53(1):014106.
84. Slavov L, Abrashev M V., Merodiiska T, Gelev C, Vandenberghe RE, Markova-Deneva I, et al. Raman spectroscopy investigation of magnetite nanoparticles in ferrofluids. J Magn Magn Mater. 2010;322(14):1904–11.
85. Chamritski I, Burns G. Infrared- And raman-active phonons of magnetite, maghemite, and hematite: A computer simulation and spectroscopic study. J Phys Chem B. 2005;109(11):4965–8.
86. Shebanova ON, Lazor P. Raman spectroscopic study of magnetite (FeFe2O4): A new assignment for the vibrational spectrum. J Solid State Chem. 2003;174(2):424–30.
87. Salviano LB, Silva Cardoso TM da, Silva GC, Silva Dantas MS, Mello Ferreira A de. Microstructural assessment of magnetite nanoparticles (Fe3O4) obtained by chemical precipitation under different synthesis conditions. Mater Res. 2018;21(2).
88. Jubb AM, Allen HC. Vibrational spectroscopic characterization of hematite, maghemite, and magnetite thin films produced by vapor deposition. ACS Appl Mater Interfaces. 2010;2(10):2804–12.
89. Yvon HJ. Raman Spectroscopy for Analysis and Monitoring. Horiba Jobin Yvon, Raman Appl Note. 2017;1–2.
90. Mitchell J. Microscopic Identification of Organic Compounds. Vol. 21, Analytical Chemistry. 1949. 448–461 p.
91. Rasouli E, Basirun WJ, Rezayi M, Shameli K, Nourmohammadi E, Khandanlou R, et al. Ultrasmall superparamagnetic Fe 3 O 4 nanoparticles: Honey-based green and facile synthesis and in vitro viability assay. Int J Nanomedicine. 2018;13:6903–11.
92. Nurbas M, Ghorbanpoor H, Avci H. An eco-friendly approach to synthesis and characterization of magnetite (Fe3O4) nanoparticles using Platanus Orientalis L. leaf extract. Dig J Nanomater Biostructures. 2017;12(4):993–1000.
93. Lobato NCC, Mansur MB, De Mello Ferreira A. Characterization and chemical stability of hydrophilic and hydrophobic magnetic nanoparticles. Mater Res. 2017;20(3):736–46.
94. Guardia P, Batlle-Brugal B, Roca AG, Iglesias O, Morales MP, Serna CJ, et al. Surfactant effects in magnetite nanoparticles of controlled size. J Magn Magn Mater. 2007;316(2 SPEC. ISS.):756–9.
95. Kemp SJ, Ferguson RM, Khandhar AP, Krishnan KM. Monodisperse magnetite nanoparticles with nearly ideal saturation magnetization. RSC Adv. 2016;6(81):77452–64.
96. Wei Y, Han B, Hu X, Lin Y, Wang X, Deng X. Synthesis of Fe3O4 nanoparticles and their magnetic properties. Procedia Eng. 2012;27(2011):632–7.
97. Millan A, Urtizberea A, Silva NJO, Palacio F, Amaral VS, Snoeck E, et al. Surface effects in maghemite nanoparticles. J Magn Magn Mater. 2007;312(1).
98. Bedanta S, Petracic O, Kleemann W. Supermagnetism. Vol. 23, Handbook of Magnetic Materials. Elsevier; 2015. 1–83 p.
99. Livesey KL, Ruta S, Anderson NR, Baldomir D, Chantrell RW, Serantes D. Beyond the blocking model to fit nanoparticle ZFC/FC magnetisation curves. Sci Rep. 2018;8(1):1–9.
100. Hedayatnasab Z, Dabbagh A, Abnisa F, Wan Daud WMA. Synthesis and in-vitro characterization of superparamagnetic iron oxide nanoparticles using a sole precursor for hyperthermia therapy. Mater Res Bull. 2020;132(May):110975.

 doi:10.20944/preprints202212.0436.v1

101. Bhardwaj A, Jain N, Parekh K. Investigating the effect of outer layer of magnetic particles on cervical cancer cells HeLa by magnetic fluid hyperthermia. Cancer Nanotechnol. 2021;12(1):1–19.
102. Jangamreddy JR, Los MJ. Mitoptosis, a novel mitochondrial death mechanism leading predominantly to activation of autophagy. Hepat Mon. 2012;12(8):10–2.
103. Yusefi M, Shameli K, Yee OS, Teow SY, Hedayatnasab Z, Jahangirian H, et al. Green synthesis of fe3o4 nanoparticles stabilized by a garcinia mangostana fruit peel extract for hyperthermia and anticancer activities. Int J Nanomedicine. 2021;16:2515–32.
104. Qing G, Zhao X, Gong N, Chen J, Li X, Gan Y, et al. Thermo-responsive triple-function nanotransporter for efficient chemo-photothermal therapy of multidrug-resistant bacterial infection. Nat Commun. 2019;10(1):1–12.